SCryPTA - SAS Crystallographic Peak Treatment and Analysis: A web-based platform for analyzing Small Angle Scattering curves of lyotropic liquid crystals.

*Raphael Dias de Castro[a], Bruna Renata Casadei[a], Barbara Vasconcelos Santana[b], Mayra Lotierzo[c], Natália F. de Oliveira[a], Barbara Malheiros[c], Renata C. K. Kaminski[b] and Leandro R. S. Barbosa[a]**

[a] Institute of Physics, University of São Paulo, USP, São Paulo, SP, Brazil, ZIP-Code 05508090.

[b] Department of Chemistry, Sergipe Federal University, Itabaiana, SE, Brazil, ZIP-Code 49500-000.

[c] Department of Biochemical and Pharmaceutical Technology, School of Pharmaceutical Sciences, USP, São Paulo, SP, Brazil, Zip-Code 05508-000

*Corresponding Author: lbarbosa@if.usp.br

ABSTRACT

Small angle X-ray scattering (SAXS) is a powerful technique for the characterization of systems with highly ordered structures, such as liquid crystals and self-assembly systems. In the field of nanotechnology and nanomedicine, SAXS can be used to characterize the crystallographic properties — namely, the space group symmetry and lattice parameter — of the crystal phase of lyotropic systems and nanoparticles with internal crystal phase, such as cubosomes, hexosomes and multi-lamellar vesicles. In this work, we introduce a new web platform named: *Small Angle Scattering Crystallographic Peak Treatment and Analysis (SCryPTA)*, capable of reading SAXS data and providing a comprehensive visualization of the scattering curve along with the calculation of important physical parameters, such as the lattice parameter of the crystal structure, the lipidic bilayer width, among others. Cubic, hexagonal and multilamellar scattering data had their crystallographic structure characterized in SCryPTA. So far, four different cubic structures, (*Pn3m* (Q_{224}), *Fd3m* (Q_{227}), *Im3m* (Q_{229}), *Ia3d* (Q_{230})), the hexagonal phase and also multi-lamellar vesicle systems are described in the software. We believe that SCryPTA may help researchers from several fields, since it has a user-friendly interface.

KEYWORDS: liquid crystals, small angle scattering analysis, diffraction data analysis, SAXS data analysis,

INTRODUCTION

Amphiphilic molecules have a large spectra of applications, being used in basic sciences as well as in nanotechnology, including live sciences and nanomedicine [1–4]. In a few and simple words, amphiphilic molecules are compounds made of at least two different regions, having one of them larger affinity to polar solvents, like water (hydrophilic region) and, at least one region with smaller affinity to polar solvents (hydrophobic region)[2]. Due to this composition, they can self-assemble spontaneously in aqueous solution into several different liquid crystalline (LC) structures[5]. Molecular geometry, molecular concentration, solvent type or changes in temperature and pH can lead to many different types of aggregates structures. In particular, lyotropic liquid crystalline (LLC) structures can be mainly classified into lamellar phase, cubic phase, and hexagonal phase according to their different internal structures (Fig. 1A – 1D).

In vivo, LLC structures are found in alveolar surface of mammalian lung [6], products of digested oil droplets in small intestine [7], thylakoid membrane in plant chloroplast [7], intracellular membranes in various cell organelles [8], wing scales or cuticle of green butterflies or beetles [9]. Some examples are applications in materials science, medical and food fields as: crystallization of proteins [10–12], DNA, SiRNA encapsulation [13], burst release for medical application [14], increase of bioavailability of lipophilic or amphiphilic compounds and control of chemical reaction (oxidation and Maillard chain reaction) in food [15,16].

In recent years, LLC phases received considerable attention because of their potential as drug delivery systems. LLC phases provide a slow drug release and protect the drug from chemical and physical degradation. Many LLC lipids are nontoxic, biodegradable and can be used for various routes of administration [17–21].

Small angle X-ray scattering (SAXS) is the most indicated technique to elucidate the polymorphism of some particular LLC structure, since it can give information on the crystallographic structure of nanometric particles [22,23].

For the lamellar phase (Figure 1A), the water domains are localized between the bilayers, this is the typical structure of systems in the presence of a small amount of water (Fig. 1A) [24].

In contrast to the lamellar phases, the normal hexagonal phase (H_I) can be regarded as elongated (prolate) or infinite cylindrical micelles, being each one surrounded by six other micelles, as schematically shown in Fig. 1B [16]. The inverse hexagonal phase (H_{II}) consists of cylindrical micelles of infinite length ordered into 2-D hexagonal arrangement in a continuous lipid matrix [16]. In H_{II} phase the packed water cylinders are surrounded by the polar head groups of the surfactant molecules and a continuum of the hydrophobic parts.

Based on X-ray crystallographic studies, the cubic phase of lipids were described in the 60s [25]. Initially, only some cubic structures were observed in the X-ray scattering curves. Later on, different cubic symmetries were observed, like the double-diamond like lattice (*Pn3m*), the body-centered lattice (*Im3m,* Figure 1C), and the gyroid lattice cubic phase (*Ia3d*). Despite the interesting properties, the application of reversed cubic phases is limited due to their high viscosity at room temperature [26,27].

SAXS is able to give information on the scattering particle structure, in particular in the nanometer range, as well as in the water channel dimension, in the case of some cubic structures and hexagonal as well [28]. An important feature of SAXS is the ability of performing measurements of systems in solution, simulating the natural environmental conditions in which the LC dispersions would be used [29]. Depending on the crystallographic arrangement of the studied system, SAXS profiles may present some, or even several peaks. These peaks reveal not only the

periodicity of the studied structure, but also its most important structural features, like unit cell parameter, for hexosomes and cubosomes, center-to-center distance for multilamellar structure, among others.

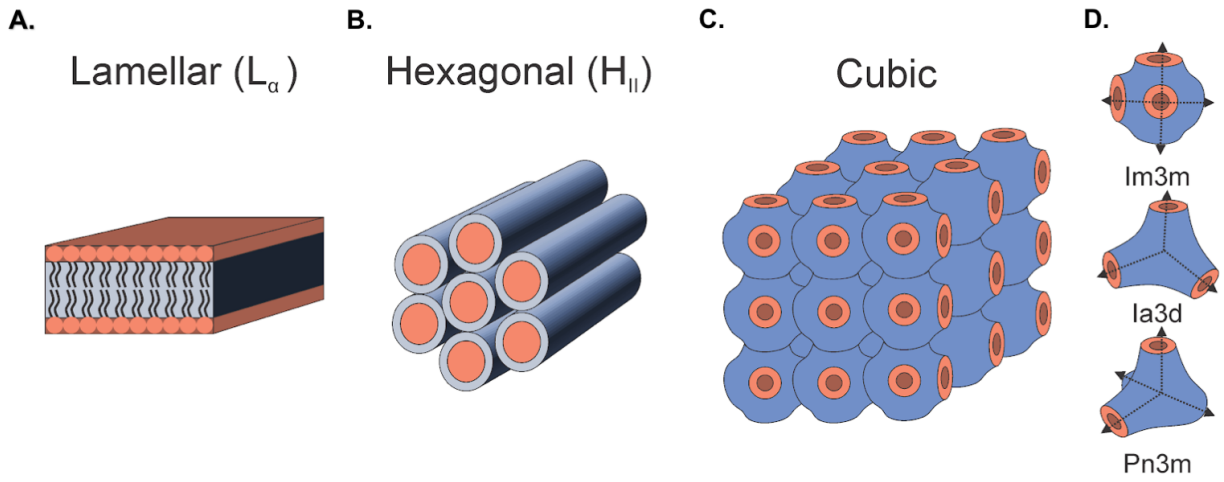

Figure 1. Schematic representation of LLC structures (A) lamellar (L_α), (B) hexagonal (H_I) and (C) cubic Im3m, (D) cubic unit cells structures of *Im3m*, *Ia3d* and *Pn3m.* The arrows indicate the direction of the water channels in Figure 1D.

Despite the large amount of research dealing with LC structures, it is not of our knowledge the existence of any web-based platform where the researcher can upload its scattering curve and get the main structural information of LLC-based systems. Thus, in the present study we report a web-based platform developed to study the structural features of LC samples, by analyzing the peaks in the SAXS curves. We have demonstrated some examples of self-assembled structures that can be treated using SCryPTA. Herein, we show that SCryPTA can describe quite well the analysis of cubic structures, hexagonal systems, multilamellar vesicles and also different systems: monoolein, phytantriol, phospholipid and natural oil, as well as it can help the researchers in the analysis of phase coexistence.

MATERIALS AND METHODS

SAMPLES PREPARATION

Fully Hydrated Monoolein: fully hydrated lipid samples were prepared by soaking monoolein (MO, glyceryl monooleate or 2,3-dihydroxypropyl oleate, Sigma Chemical Co., with >99% purity and used without further purification, St. Louis, MO) into the appropriate amount of ultrapure Milli-Q water (resistivity of 18.2 MΩ.cm at 25 °C). MO final concentration was set to c_{MO} = 25 mg/mL. After preparation, MO samples were vortexed and left for equilibration for 4 hours before the measurements.

Cubosomes and *Hexosomes:* samples prepared with phytantriol (PHY, 3,7,11,15- tetramethyl-1,2,3-hexadecanetriol, Sigma Chemical Co., St. Louis, MO) and Pluronic F-127 (F127, Sigma Chemical Co., St. Louis, MO) were based on bottom-up methodology, studied by Akhlaghi et al.[30]. Briefly, two solutions were produced, the first one 100 mg of PHY was solubilized into 10 mL of ethanol. Then, 25 mg of F127 was solubilized in 22.5 mL of ultrapure water. Subsequently, lipid solution was dropwise into the F127, at 45 ºC (above fusion point). The final solution was brought to a rotary evaporator until the final volume was 5 mL. In order to produce the hexosomes, 0.1 mM of chloroform was added in the regular cubosome sample (as described above).

Liposomes: samples were prepared by solubilizing the desired amount of POPC (1-palmitoyl-2-oleoyl-*sn*-glycero-3-phosphocholine, Avanti Polar Lipids, Alabaster, AL) in chloroform. The solvent was evaporated from the sample with a continuous flow of ultra-pure N_2 forming a lipid film in the test tubes. Then, to ensure no solvent residue, the film was stored at low pressure (inside desiccator, using a vacuum pump) for 2 hours for complete evaporation of the organic solvent.

Ultrapure water was added to the test tube, and multilamellar vesicles (MLVs) were formed by mechanical agitation of the tube (2 min of vortex mixing) at 10 mM.

Amazonian rainforest oils: liquid-crystalline formulations based in Amazonian rainforest oil were prepared in the presence of Polysorbate 80 (TWEEN 80, from Dinâmica Contemporânea, Sào Paulo, Brazil) as surfactant, *Pentaclethra macroloba* oil (Pracachy oil PO, from Amazon oil) as the oil phase, and ultrapure water (H_2O) at ratio 50 surfactant : 10 oil : 40 water (w:w:w). All the components were mixed manually. Formulations were stabilized at room temperature by 18 hours and stored at 15 °C.

Small Angle X-ray Scattering Measurements

SAXS experiments were performed at beamline D01B, SAXS1 at the Brazilian Synchrotron Light Laboratory (LNLS), Campinas – SP/Brazil. Beam wavelength of the synchrotron source was reported to be 1.488 Å and the sample-detector distance was set to ~1000 mm. Time acquisition for each sample was set to 100 s and several frames were measured in order to check for radiation damage. This effect was not evidenced in the present study. All measurements (unless otherwise mentioned) were performed at room temperature (22.0 ± 0.5 ºC) controlled with a water-bath. Finally, 2D images (obtained with a 300K Pilatus detector, Dectris, Switzerland) were radially averaged and the contribution of the buffer solution was subtracted taking into account the sample's attenuation.

SAXS Overview

Small Angle X-ray Scattering (SAXS) technique is a very useful tool in the study of colloidal particles as it allows the measurement of size, shape and possible interactions between the scattering particles. There is an inverse relationship between wavelength and particle size under study. For X-ray wavelengths (on the order of 1 - 2 Å) particle sizes may range from about 10 - 20 Å to about 400 - 500 Å, depending on the experimental arrangement.

A typical setup for SAXS experiment can be appreciated on Fig. 2A. SAXS technique is based on the scattering of X-rays, interacting with the sample. The incident beam ($\vec{k}_i$) hits the sample and is scattered ($\vec{k}_o$) reaching the detector at some specific position, while it also passes through the sample ($\vec{k'}_i$), being known as the direct beam (Fig. 2A). The angle between ($\vec{k'}_i$) and the scattered photon, ($\vec{k}_o$), is defined as 2θ, Fig. 2B.

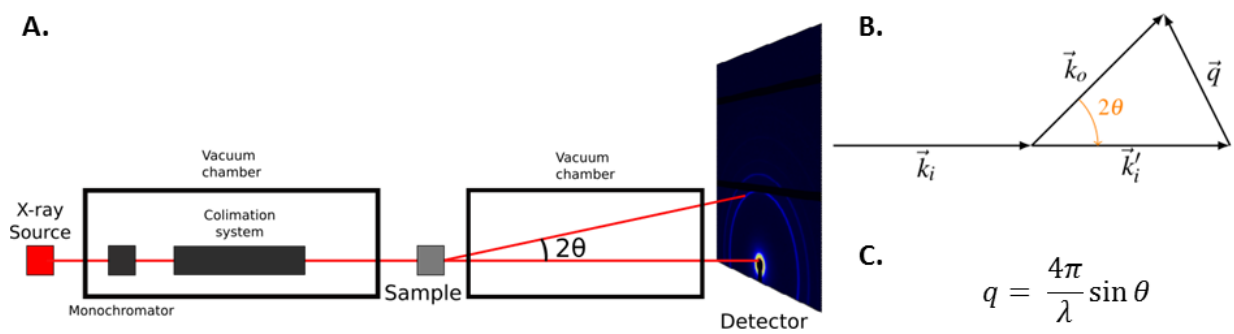

Figure 2. A) Schematization of small angle X-ray scattering experiment. **B)** Definition of the scattering vector, ($\vec{q}$), **C)** Definition of the scattering vector modulus, $|\vec{q}|$.

The scattering vector ($\vec{q}$) is thus defined as the difference between the scattered ($\vec{k}_o$) and the transmitted photons directions ($\vec{k'}_i$) (Fig. 2B). SAXS output data will then relate X-ray elastic

scattering intensity with values of the magnitude of $\vec{q}$, determined mathematically by simple geometric deduction (Fig. 2C), given that $\vec{k}_i = \vec{k}_o = \vec{k'}_i = \frac{2\pi}{\lambda}$, being λ the radiation wavelength.

METHODOLOGY

SAXS

Bragg diffraction at small angles

The main underlying concept of SAXS technique is the scattering of X-rays by electrons of the atoms in a crystal lattice. There are several studies and textbooks elucidating the interaction of X-rays with matter. It is not the scope of this manuscript to do so. The reader can find all of that information elsewhere [31,32]. Herein we will focus our attention on the LC X-ray patterns, in particular for those systems that were implemented in SCryPTA.

In particular for cubic structures, the distance between the reflection planes, d_{hkl}, is related to the lattice parameter (or unit cell parameter) a, which is the repetition distance of the crystal lattice. Both quantities are related by:

$$d_{hkl} = \frac{a}{\sqrt{h^2 + k^2 + l^2}} \quad (1)$$

where h, k and l are the Müller indices, indicating the allowed Bragg reflection planes for such structures.

Each diffraction peak in the scattering curve can be assigned to a specific distance (d) that characterize this reflection plane. Equation 2 shows the relationship among the peak position, the unit cell parameter and the reflection plane (hkl):

$$q = \frac{2\pi}{a}\sqrt{h^2 + k^2 + l^2} \quad (2)$$

The interpretation of these numbers (*hkl*) can lead to the identification of the space group related to the crystal structure of the sample. Table 1 shows the allowed Bragg reflections for *Pn3m*, *Fd3m*, *Im3m* and *Ia3d* cubic phases, as well as for the lamellar and hexagonal structures.

Thus, using the position of each peak on the SAXS curve, one can find the relationship among them. Since each peak is related to a value of the scattering vector (each peak can be labeled as q_1, q_2, q_3 and so on), it is possible to calculate the ratios between the i_{th} peak (q_i) and q_1 as follows:

$$\left.\begin{aligned} q_i &= \frac{2\pi}{a}\sqrt{h_i^2+k_i^2+l_i^2} \\ q_1 &= \frac{2\pi}{a}\sqrt{h_1^2+k_1^2+l_1^2} \end{aligned}\right\} \quad \Longrightarrow \quad \frac{q_i}{q_1} = \sqrt{\frac{h_i^2+k_i^2+l_i^2}{h_1^2+k_1^2+l_1^2}} \tag{3}$$

Equations 3 allows the calculation of the ratios between the Bragg reflections for each space group (see Table 1), defining a method for the crystal lattice identification. For instance, in the case of *Im3m* and *Pn3m* (Equation 4), the first two ratios are:

$$\begin{aligned} Im\bar{3}m \quad &\rightarrow \quad \frac{q_2}{q_1} = \sqrt{2} \qquad \frac{q_3}{q_1} = \sqrt{3} \\ Pn\bar{3}m \quad &\rightarrow \quad \frac{q_2}{q_1} = \sqrt{\frac{3}{2}} \qquad \frac{q_3}{q_1} = \sqrt{2} \end{aligned} \tag{4}$$

Table 1 – The allowed reflection planes (with the Müller indices) for the six symmetries used in SCryPTA.

Reflection (hkl)	**Lamellar**	**Hexag.****	**Pn3m (Q_{224})***	**Fd3m (Q_{227})***	**Im3m (Q_{229})***	**Ia3d (Q_{230})***
100	$\sqrt{1}$	$\sqrt{1}$	-	-	-	-
110	-	$\sqrt{3}$	$\sqrt{2}$	-	$\sqrt{2}$	-
111	-	-	$\sqrt{3}$	$\sqrt{3}$	-	-
200	$\sqrt{4}$	$\sqrt{4}$	$\sqrt{4}$	-	$\sqrt{4}$	-
210	-	$\sqrt{6}$	-	-	-	-
211	-	-	$\sqrt{6}$	-	$\sqrt{6}$	$\sqrt{6}$
220	-	$\sqrt{12}$	$\sqrt{8}$	$\sqrt{8}$	$\sqrt{8}$	$\sqrt{8}$
221	-	-	$\sqrt{9}$	-	-	-
300	$\sqrt{9}$	$\sqrt{9}$	-	-	-	-
310	-	$\sqrt{13}$	$\sqrt{10}$	-	$\sqrt{10}$	-
311	-	-	$\sqrt{11}$	$\sqrt{11}$	-	-
222	-	-	$\sqrt{12}$	$\sqrt{12}$	$\sqrt{12}$	-
320	-	$\sqrt{19}$	-	-	-	-
321	-	-	$\sqrt{14}$	-	$\sqrt{14}$	$\sqrt{14}$
400	$\sqrt{16}$	$\sqrt{16}$	$\sqrt{16}$	$\sqrt{16}$	$\sqrt{16}$	$\sqrt{16}$

410			-	-	-	-
411	-	-	$\sqrt{18}$	-	

Legend: **Hexag.** refers to hexagonal symmetry. * The numbers indicated for each cubic crystallographic space group are calculated with $\sqrt{h^2 + k^2 + l^2}$ along with each allowed reflection for each symmetry. ** The numbers indicated for each cubic crystallographic space group is calculated with $\sqrt{h^2 + k^2 + hk}$.

The same procedure may be applied to lamellar and hexagonal phases by SCryPTA. For instance, as in the case of the cubic symmetries, the scattering vector is proportional to an irrational number calculated with $\sqrt{h^2 + k^2 + hk}$, where h and k are related to the Muller indices of the allowed Bragg reflections of the hexagonal phase. Therefore, the hexagonal phase has allowed Bragg reflections that can be assigned to 1, $\sqrt{3}$, $\sqrt{4}$, $\sqrt{7}$, $\sqrt{9}$, $\sqrt{12}$ and so on (see Table 1), and the lattice parameter can be calculated using the value of the scattering vector with Equation 5.

$$q_{hex} = \frac{4\pi}{\sqrt{3}} \frac{\sqrt{h^2 + k^2 + hk}}{a_{hex}} \tag{5}$$

The peaks present in the scattering pattern of multi-lamellar phases have a uniform spacing and the lattice parameter is inversely proportional to the magnitude of the scattering vector ($a = 2\pi/q_{peak}$).

In the present study, it is not our goal to provide a detailed analysis of X-ray of LC Phases. There is a large amount of research and textbooks dealing with these theories. Herein we present a new tool to help researchers to treat and analyze their scattering data. To do so, some explanations on the SCryPTA computational tools are necessary.

SAXS analysis with the computational tools

SCryPTA was developed using a Python-based interface, taking advantage of the features of the Jupyter platform. Thus, this web-based application uses well-known Python libraries, such as Numpy, Scipy, Matplotllib and Bokeh, and also a specific peak detection function also developed with Python.

The calculations performed to obtain the lattice parameter a and all the other derived parameters use a Gaussian fit based procedure. Nevertheless, the user must know that this is an approach and it is quite often that diffraction peaks have no Gaussian profile. Even though, since the peaks for LC Phases are not so narrow as compared to metal-like crystals, for instance, this procedure does not induce any significant error on the derived parameters.

SCryPTA uses a Gaussian function to fit the data of the first peak diffraction, by selecting a region around this peak. By doing so, it is possible to get the unit cell parameter for the LC phase. Depending on the LC phase, it will be possible to calculate several physicochemical properties, as follows:

Pn3m (Q_{224}), Ia3d (Q_{229}) and Im3m (Q_{230})

There are several studies in the literature describing cubic structures for lipids [12,27,33,34]. The structure of four of them (*Pn3m*, *Im3m*, *Ia3d* and *Fd3m*) can be described in terms of networks of cylinders, connected in different ways: in *Pn3m* the cylinders are tetrahedrally joined 4 by 4, similar to the diamond structure; for *Ia3d* the cylinders are coplanarly joined 3 by 3; and finally for *Im3m* the cylinders are cubically joined 6 by 6 [27]. Regarding the *Fd3m* structure, it is related to

the *Pn3m*, but in this case one of the cylinders network is replaced by a lattice of closed micelles, whereas the other network is kept unaltered [27].

SCryPTA can calculate some of the physicochemical properties of these cubic structures. For *Pn3m* and *Im3m*, SCryPTA can calculate the water channel (cylinder) radius (r_w) and the length of the lipid molecule that forms the bilayer (l_L), i.e, roughly half the length of the lipidic bilayer. In the case of the water channel radius, the following formulas reported in the literature were used[35,36]:

$$r_w^{(Pn3m)} = 0.391a - l_L \tag{6}$$

$$r_w^{(Im3m)} = 0.305a - l_L \tag{7}$$

where r_w is the water channel radius, a is the lattice parameter of the respective cubic structure and l_L is the length of the lipid molecule in the bilayer, which in turn can be deduced from the lipid volume fraction ϕ_L formula [21,37]:

$$\phi_L = 2A_0\frac{l_L}{a} + \frac{4\pi}{3}\chi\left(\frac{l_L}{a}\right)^3 \tag{8}$$

Equation 8 depends on two constant parameters related to the cubic phase: A_0 is the ratio of the area of the minimal surface in the unit cell to the quantity ([*unit cell volume*]$^{2/3}$) and χ is the Euler–Poincare characteristic [36], which is an invariant describing the topological space shape [21,37]. These values for the *Pn3m*, *Im3m* and *Ia3d* structures are presented in Table 2.

Table 2 – Values for the cubic minimal surface parameters [21].

Cubic phase	A_0	χ
Pn3m	1.919	-2
Im3m	2.345	-4
Ia3d	3.091	-8

From Equation 8, l_L can be determined as one of its solutions [37], as described in Equation 9:

$$l_L = \frac{a}{2}\sqrt{\frac{8A_0}{\pi|\chi|}}\cos\left\{\frac{1}{3}\left[\pi + \arccos\left(\phi_L\sqrt{\frac{9\pi|\chi|}{8A_0^3}}\right)\right]\right\} \tag{9}$$

SCryPTA can thus calculate some of these parameters, helping the researcher to describe their systems or even helping in better understand the influence of some external parameters on the internal cubic structure under evaluation.

In addition to the cubic structure, SCryPTA can also calculate some important parameters for lamellar and hexagonal structures, such as the unit cell parameter. To date, the web-platform has been developed primarily for the study of cubic structures and more tools for studying hexagonal and lamellar symmetries are under development.

Software Workflow

SCryPTA's interface relies on the execution of several steps using the Jupyter notebook interface. Fig. 3 shows an overview of application's workflow. Briefly, this tool can read and perform calculations from SAXS experimental data in which diffraction peaks are distinguishable from background scattering. The main function of this application is to identify the crystallographic symmetry present in the scattering pattern, and an optional peak detection function can be enabled to calculate some physical parameters, such as the lattice parameter.

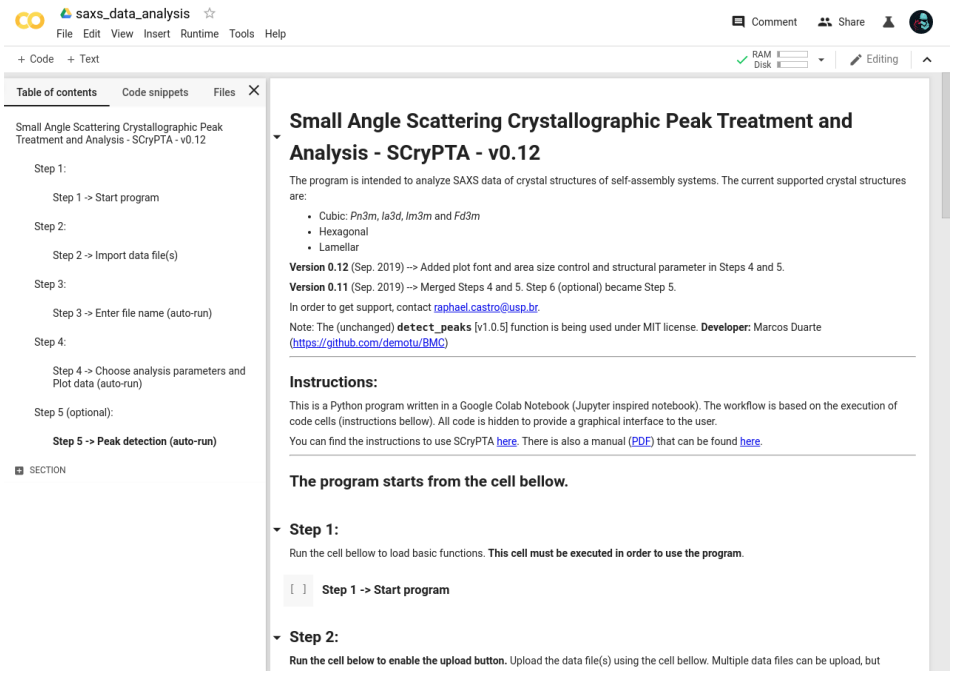

Figure 3. SCryPTA's interface is based on the Jupyter notebook. Each step of the application can be executed independently after the basic functions are initiated.

The most basic feature of SCryPTA is to provide easy and fast data visualization on the site of the experiment, which could be performed, right after the data acquisition, since the software just requires an internet connection. Thus, using basic functions of Python's Matplotlib and Bokeh

libraries, SCryPTA produces an interactive plot that enables one to explore the dataset collected at real-time right after the measurements.

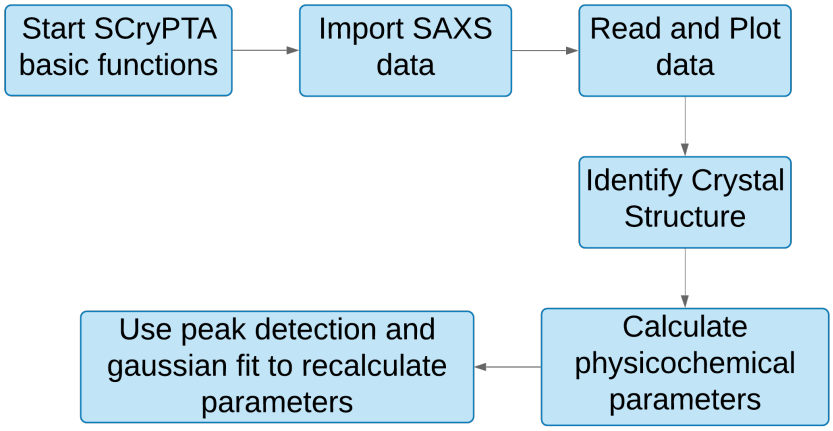

Figure 4. SCryPTA flowchart with major processes in data analysis, composed of five parts: import SAXS data, read/plot data, identify crystal structure, use peak detection and gaussian fit to calculate parameters and plot data and show results.

In order to identify the crystal structure present in the sample, SCryPTA provides an easy procedure (Fig. 4). The user has the option to perform a visual "initial guess" for the position of the first peak, i.e., the magnitude of the scattering vector q of the first diffraction peak, by indicating the value of q in the software interface and also choosing a specific symmetry available in the platform (four cubic, hexagonal and multi-lamellar). The value of q can be visualized with the interactive plot interface. SCryPTA will automatically plot lines indicating the expected position of the following 6 peaks, providing a "visual fit" of the expected diffraction peaks position. If these lines are aligned with the peaks of the diffraction pattern, then the crystal lattice can be identified. This process is represented in Fig. 5.

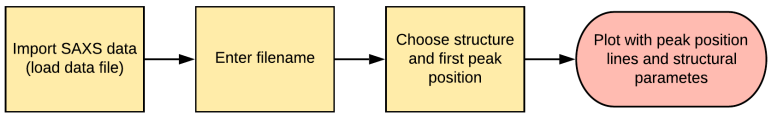

Figure 5. Process for crystal lattice identification on SCryPTA has four steps: load data, enter filename with data to be analyzed, choose structure and first peak position, and finally generate plot.

In addition to the identification of the crystal lattice, the process described above also provides the results of calculations for the lattice parameter of all available structures, along with lipid length in the bilayer and water channel diameter for the cubic phases. These calculations are performed using the first peak position indicated by the user. This is a first approach to characterize the system related to the analyzed data.

If the process described above is successful, the user has a first and quick identification in the analyzed system. However, SCryPTA can also provide a more accurate characterization using the implemented peak detection and fit functions. By automatically detecting the diffraction peaks present in the dataset, SCryPTA performs a gaussian fit to these peaks, generating the "fitted" position for each peak, with their respective uncertainties. These values are then used to calculate structural parameters for the selected structure. The workflow of this process is presented in Fig. 6.

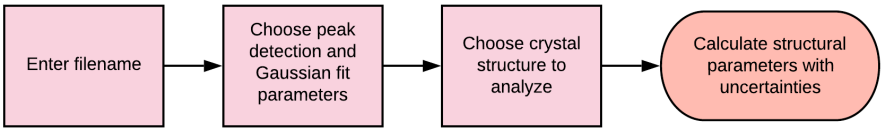

Figure 6. An additional characterization process is provided in SCryPTA, where the user can calculate more accurate values for the structural parameters of the analyzed structure.

In order to produce a clear manuscript, the detailed use of SCryPTA can be visualized in the web-page manual, which is constantly updated as new versions of ScryPTA are released. (http://fig.if.usp.br/~scrypta/Manual_SCryPTA.pdf). In the following section, we demonstrate how SCryPTA can be used to study LC systems, by showing some examples.

RESULTS AND DISCUSSION

In this section, some results obtained using SCryPTA are presented. Besides these examples, the reader can find more information on SCryPTA on the website (www.if.usp.br/scrypta). Initially, SCryPTA was implemented with four different cubic structures: (*Pn3m* (Q_{224}), *Fd3m* (Q_{227}), *Im3m* (Q_{229}), *Ia3d* (Q_{230})) besides the hexagonal and lamellar phases. New structures can be added in the future, by demand.

1. Cubic Structures

Monoolein

Monoolein (MO) is a nontoxic, biodegradable and biocompatible material and well-known emulsifying agent and food additive since the 1950s [38,39]. Despite being a simple lipid structure (Fig. 7), it exhibits a rich phase diagram depending on its concentration and temperature [40–42]. It presents ordered lamellar phase (~0 °C), reversed micellar, lamellar, reversed bicontinuous cubic phases (*Im3m* and *Pn3m*), at room temperature, and a reverse hexagonal phase at higher temperatures (~85 °C) [42].

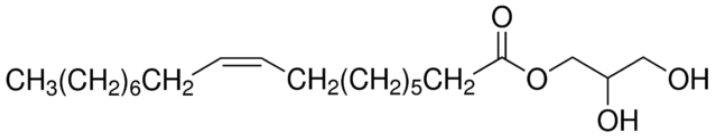

Figure 7. Molecular structure of Monoolein.

Besides its rich phase diagram, it is known that MO can have different structure in the presence of other molecules. For instance, Mariani et al. [27] studied the structure of cubic phases of MO in the absence and presence of cytochrome-c, a water soluble protein found in the mitochondria with

key role in the cell respiration[27]. Later on, Mazzoni et al.[21] also studied the effect of cytochrome-c on MO phase diagram as a function on protein concentration, temperature and pressure[21]. The authors have shown that different concentrations of cytochrome-c in solution triggered a transition from *Pn3m* to *Im3m* (2 proteins per unit cell) cubic phases and from *Im3m* to $P4_332$ cubic phase (10 to 20 proteins per unit cell)[21]. They also have shown that, at room temperature, the lattice parameter values were 10.60 nm for the *Pn3m* phase and 12.17 nm for the *Im3m* phase [21].

Here we present the analysis performed on the scattering data of the MO-water system in absence (Fig. 8A) and presence (Fig. 8B) of cytochrome-c. SCryPTA was able to identify the *Pn3m* cubic phase of the MO-water system in the absence of protein (Fig. 8A), providing a lattice parameter of 10.55 ± 0.08 nm which is in agreement with the original results [20,21,27]. The lipidic bilayer length and the water channel diameter were also calculated, being 4.366 ± 0.032 nm and 3.884 ± 0.029 nm, respectively.

In the case of the MO-cytochrome c-water system, SCryPTA identified the *Im3m* phase (Fig. 8B) and provided results for the lattice parameter, lipidic bilayer length and water channel diameter: 12.43 ± 0.11 nm, 3.453 ± 0.003 nm and 4.13 ± 0.07 nm, respectively. Those results are also in good agreement with the one reported by Mazzoni et al.[21].

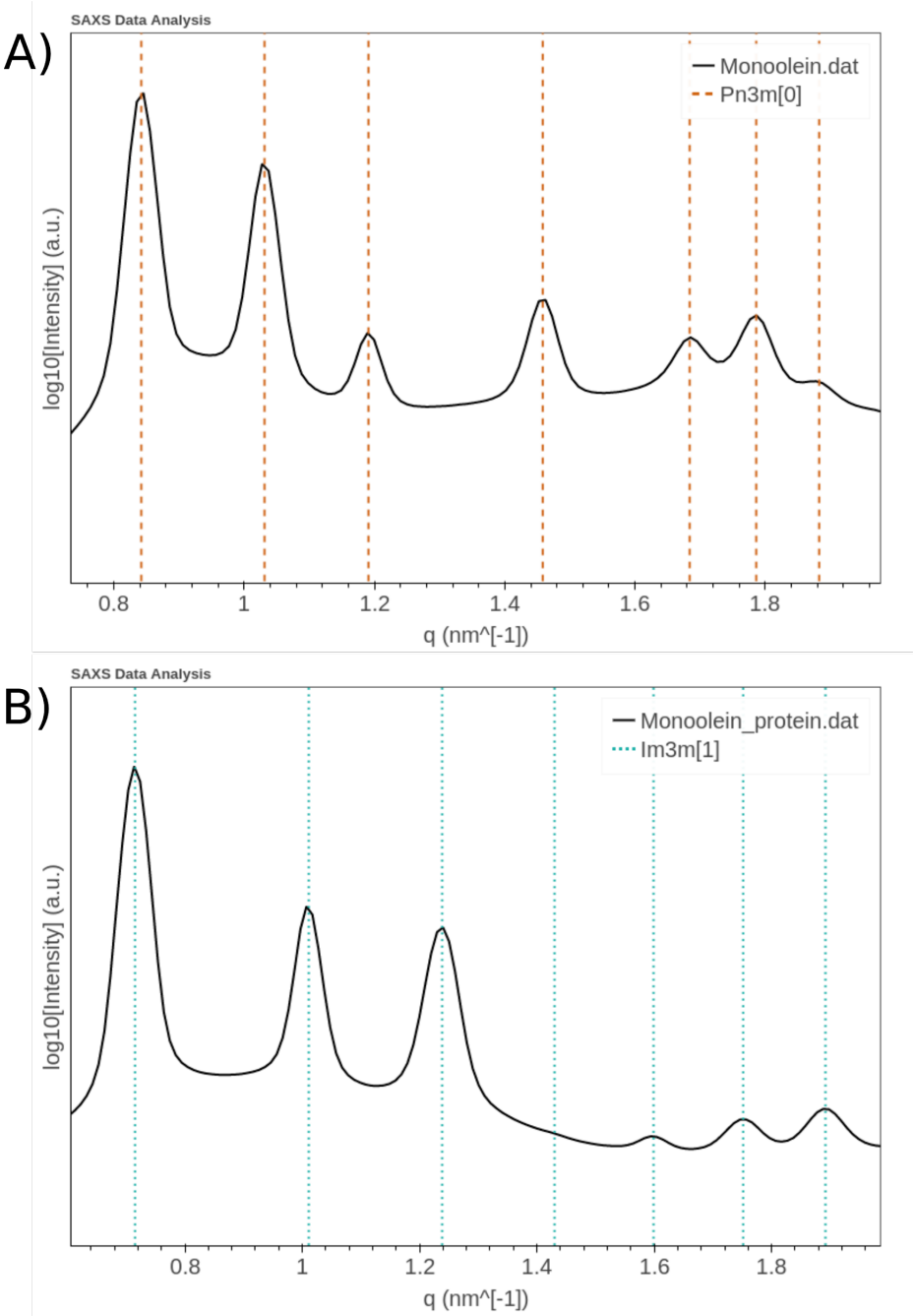

Figure 8. A) Scattering pattern of the MO-water system in the absence of cytochrome-c. SCryPTA was able to confirm the presence of the *Pn3m* phase in such system. **B)** When the protein is present in the same system, there is a clear transition to the *Im3m* cubic phase.

As shown in Fig. 8 (A and B) SCryPTA was able to correctly describe the cubic phase of MO in the absence and presence of cytochrome-c. Besides these structures, SCryPTA was also tested with other symmetries, as follows.

Cubosomes (Pn3m)

Phytantriol (PHY) is a well-known active ingredient used in the cosmetic industry, such as hair and skin care products. PHY exhibits similar phase behavior to MO [43] and has gained more recent interest in the biomedical field compared to monoglycerides due to several reasons, such as chemical stability due to the absence of the ester group and can be purchased commercially with high purity (~95%) [33,43,44].

On the other hand, cubosomes are lipidic nanoparticles, with cubic inner structure [20,33,44], they have shown interesting physicochemical properties and are being considered quite interesting as drug delivery systems [20,45,46]. These quite novel and interesting material have a higher hydrophilic surface area, making it a quite interesting material for drug delivery systems [47].

The amphiphilic and non-ionic polymer Pluronic® F127 has a quite interesting behavior in the PHY physical properties. Under some specific conditions, stable cubosomes can be produced combining PHY and F127 [44].

Fig. 9 shows the SAXS curves of cubosomes composed of PHY, in the presence of the amphiphilic polymer Pluronic® F127. As one can see, six well defined peaks are present in the scattering pattern. Once the user defines the position of the first peak, SCryPTA can calculate the predicted positions of the next six peaks, according to crystallographic structure also chosen by the user. Fig. 9 shows the predicted peak positions of the *Pn3m* (vertical red lines) and *Ia3d*

(vertical green lines) cubic phases. The first peak of both structures was defined at q_1 = 1.32 nm^{-1}. As one can see in Fig. 9, the *Ia3d* structure (green lines) is not able to describe the experimental diffraction peaks, indicating that Ia3d cubic structure is not appropriate to describe this system.

Concerning *Pn3m* structure, one can see that the position of all six diffraction peaks can describe satisfactorily using such symmetry (vertical red lines in Fig. 9).

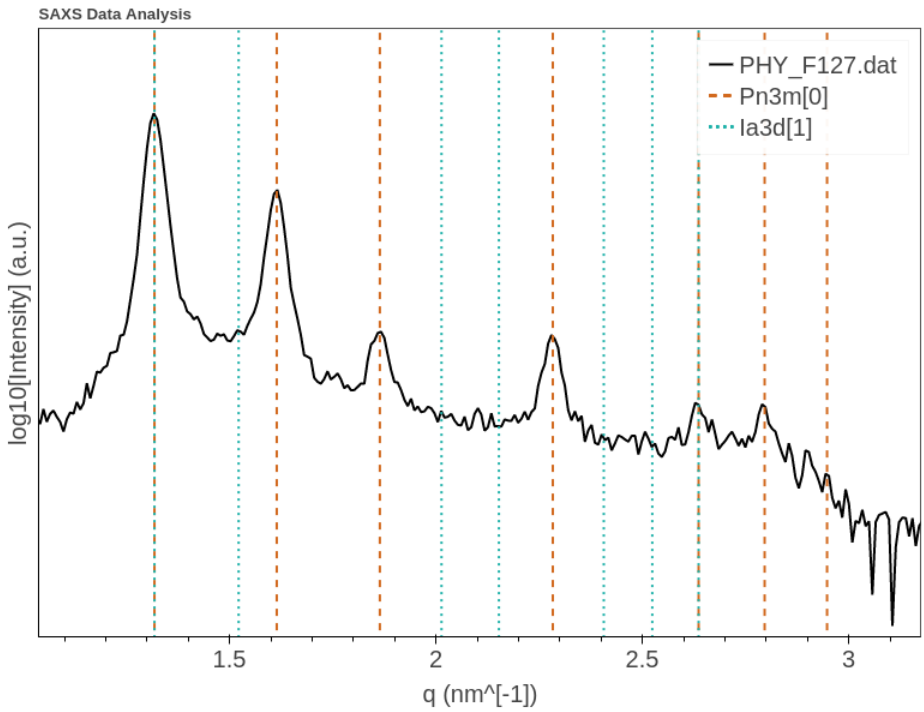

Figure 9. Experimental scattering curve of cubosomes, composed by phytantriol in the presence of F127 non-ionic amphiphilic polymer. Two possible cubic structures are also shown, *Ia3d* (red lines) and *Pn3m* (green lines).

SCryPTA performed calculations of the structural parameters of the *Pn3m*. The lattice parameter was evaluated calculated as 6.74 ± 0.04 nm, in accordance with the results predicted in the literature [49]. Also, two other important results were obtained: lipidic bilayer length at 2.792 ± 0.016 nm and water channel diameter at 2.482 ± 0.014 nm.

2. **Hexagonal**

Nonpolar organic solvents have been widely reported as a convenient method used to dissolve hydrophobic bioactive molecules [48–51]. Nevertheless, due to its hydrophobic nature, it may induce changes in nanoparticles depending on its concentration. Fig. 10 shows the SAXS diffraction pattern of PHY cubosomes in the presence of chloroform at 0.1 mM. A phase transition from cubic *Pn3m* (see Fig. 9) to hexagonal (Fig. 10) was verified using SCryPTA. The lattice parameter of the hexagonal phase was also provided by the application: 4.755 ± 0.026 nm.

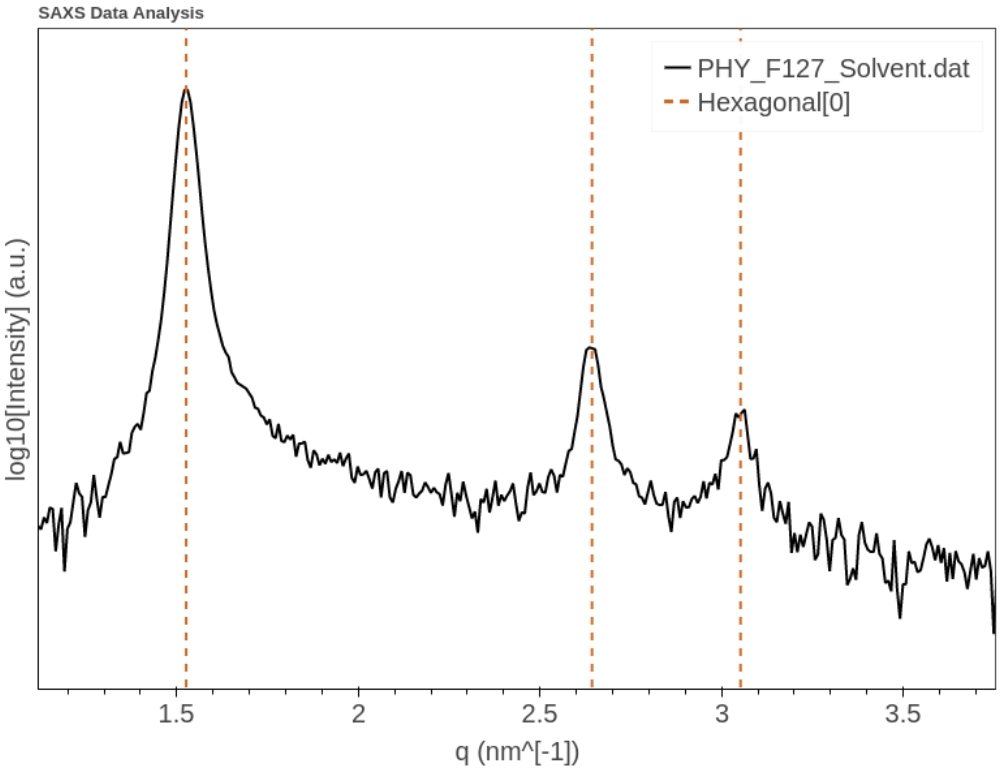

Figure 10. SAXS curves of aqueous solution of cubosomes, composed of PHY, Pluronic F127 in the presence of 0.1 mM of chloroform. The red lines represent the theoretical peak positions of an hexagonal arrangement with inner lattice parameter of 4.755 ± 0.026 nm.

3. Multilamellar (MLVs)

Multilamellar vesicles (MLVs) are spherical concentric vesicles composed by several lamellar lipid bilayers. Fig. 11 shows the SAXS curve of multilamellar vesicles composed by 10 mM of POPC. SCryPTA was able to identify the multilamellar phase in the samples, and also calculated the lattice parameter as 6.35 ± 0.04 nm. Similar values are reported in the literature [52,53]. In this case, the lattice parameter is interpreted as the center-to-center average distance between two consecutive bilayers.

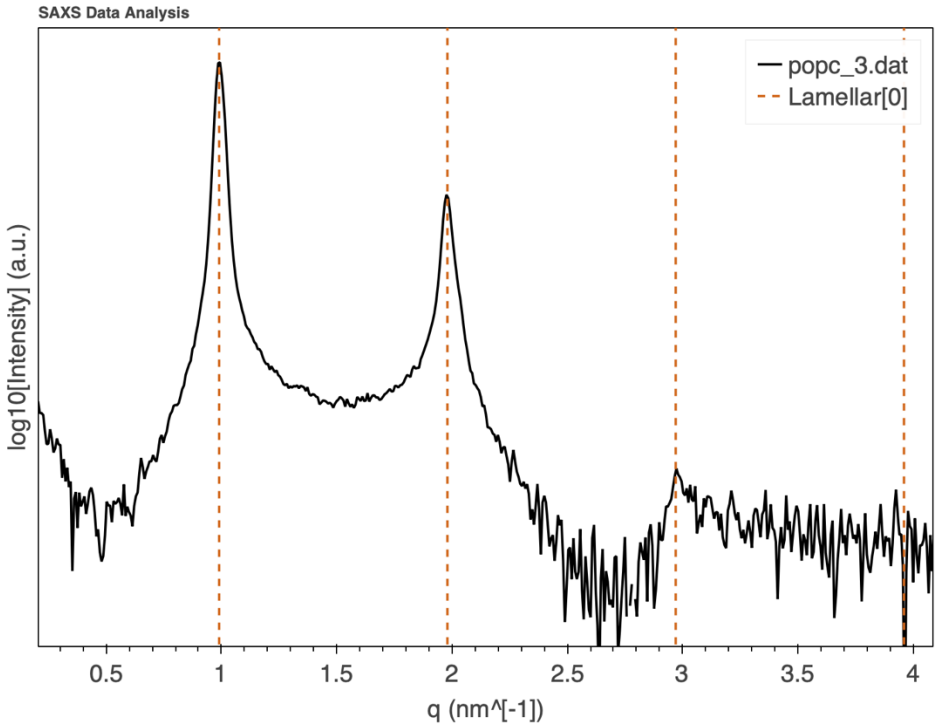

Figure 11. SAXS curve of multilamellar vesicles composed by POPC at 10 mM in ultrapure milli-Q water.

4. Phase Coexistence

SCryPTA is able to describe the coexistence of crystallographic phases. Fig. 12 shows the SAXS curve of two phases coexisting in a system obtained from the mixture of 50% of TWEEN 80, 10% of Pracachy oil and 40% of water (w:w:w). Pracachy oil is a not well studied cosmetic oil extracted from the seeds of *Pentaclethra macroloba* tree, which grows in Amazonian rainforest at Panamá, Nicaragua and Brazil. It has interesting properties like antifungal, anti-inflammatory and anti-bacterial effects [54]. Besides that, it also presents capacity to heal scars fast [55] and also has repellent effect against *Aedes aegypti*. Polysorbates (Tweens) are the most used surfactants, presenting a sorbitan ring with a hydrophilic region of polyoxyethylene groups and a hydrophobic region of sorbitan fatty esters. TWEEN 80 is a well-known polysorbate frequently used in cosmetics and food. It has a well-studied structural behavior in aqueous solutions, forming micellar systems and gel-like LC structures, influenced by external factors such as pH, temperature, pressure and additives as oils and co-surfactants. Accordingly, all the scattering peaks can be represented as a sum of a cubic (*Fd3m*) with lattice parameter of 17.25 nm, and a hexagonal with unit cell of 21.99 nm (Fig. 12).

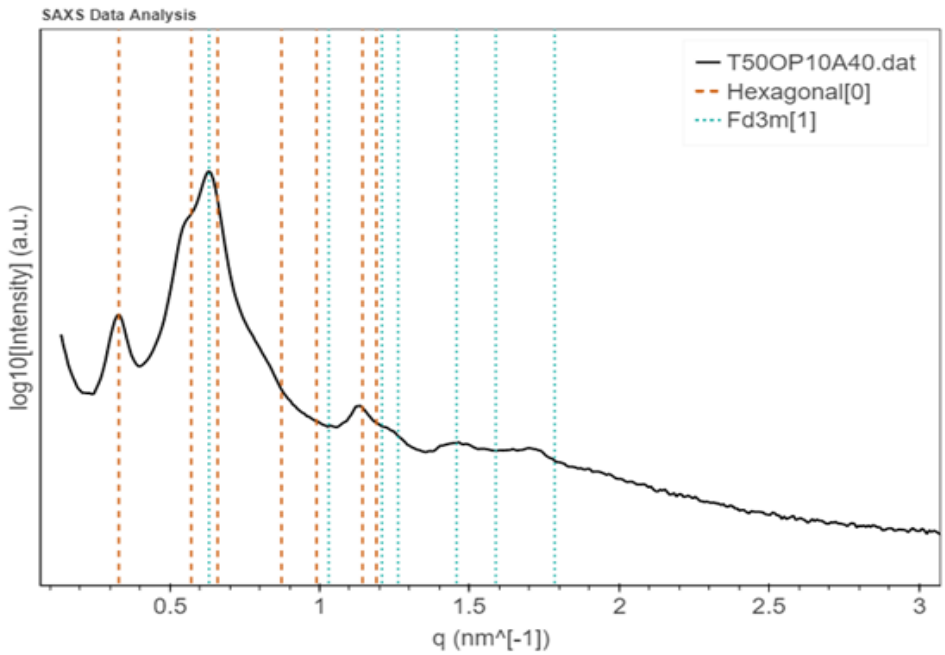

Figure 12. SAXS curve of the mixture: 50% of TWEEN 80, 10% of Pracachy oil and 40% of water (w:w:w). Vertical lines indicates the presence of two structures: Hexagonal (red lines) and Fd3m (green lines).

CONCLUSIONS

In this study we showed a web-based platform that can be used to analyze small angle scattering curves of LC samples. As we have shown along this manuscript, SCryPTA can successfully describe the main structural features of LLC, with a user-friendly interface and calculating important structural features. So far, SCryPTA can be used to describe four different cubic structures (*Pn3m* (Q_{224}), *Fd3m* (Q_{227}), *Im3m* (Q_{229}), *Ia3d* (Q_{230})) and both Hexagonal phases (normal H_I, and inverted H_{II}) and the Multilamellar stacking. In this version of SCryPTA it is also possible to elucidate a mixture of structures in the same sample given the structural parameters of each one. Nevertheless, it should be stressed that SCryPTA is not able to calculate the percentage of each structure, but only the respective structural parameters. We believe that SCryPTA can be used by several different researchers, from nanostructured drug-delivery systems, including nanomedicine, engineering, food science, oil industry and technology.

ACKNOWLEDGMENTS

Financial support for this research was provided by Fundação de Amparo à Pesquisa do Estado de São Paulo (FAPESP) (2015/15822-1, 2019/08832-1, 2018/04796-8), CAPES, CNPq (#155970/2018-6, 308692/2018-7, 420567/2016-0) and FAPITEC are also acknowledged. BRC, BVS, BM, ML and LRSB thanks CNPq for research grant. A special thanks to the National Laboratory of Synchrotron Light (LNLS), SAXS-1 beamline, and National Laboratory of Nanotechnology (LNNano), Campinas-SP, for the usage of their facilities.

REFERENCES

(1) Tadros, T. Self-Assembly of Surfactants. In *Encyclopedia of Colloid and Interface Science*; Tadros, T., Ed.; Springer Berlin Heidelberg: Berlin, Heidelberg, 2013; pp 1044–1044.

(2) Heerklotz, H. Interactions of Surfactants with Lipid Membranes. *Q. Rev. Biophys.* **2008**, *41*, 205–264.

(3) Lawrence, M. J. Surfactant Systems: Their Use in Drug Delivery. *Chem. Soc. Rev.* **1994**, *23*, 417–424.

(4) Ranneh, A.-H.; Iwao, Y.; Noguchi, S.; Oka, T.; Itai, S. The Use of Surfactants to Enhance the Solubility and Stability of the Water-Insoluble Anticancer Drug SN38 into Liquid Crystalline Phase Nanoparticles. *Int. J. Pharm.* **2016**, *515*, 501–505.

(5) Israelachvili, J. N. Intermolecular and Surface Forces: Revised Third Edition. *Acad. Press.* **2011**.

(6) Larsson, M.; Terasaki, O.; Larsson, K. A Solid State Transition in the Tetragonal Lipid Bilayer Structure at the Lung Alveolar Surface. *Solid State Sci.* **2003**, *5*, 109–114.

(7) Selstam, E.; Schelin, J.; Williams, W. P.; Brain, A. P. R. Structural Organisation of Prolamellar Bodies (PLB) Isolated from Zea Mays. Parallel TEM, SAXS and Absorption Spectra Measurements on Samples Subjected to Freeze-Thaw, Reduced PH and High-Salt Perturbation. *Biochim. Biophys. Acta - Biomembr.* **2007**, *1768*, 2235–2245.

(8) Almsherqi, Z. A.; Landh, T.; Kohlwein, S. D.; Deng, Y. Chapter 6: Cubic Membranes the Missing Dimension of Cell Membrane Organization. *Int. Rev. Cell Mol. Biol.* **2009**, *274*, 275–342.

(9) Wilts, B. D.; Apeleo Zubiri, B.; Klatt, M. A.; Butz, B.; Fischer, M. G.; Kelly, S. T.; Spiecker, E.; Steiner, U.; Schröder-Turk, G. E. Butterfly Gyroid Nanostructures as a Time-Frozen Glimpse of Intracellular Membrane Development. *Sci. Adv.* **2017**, *3,* .

(10) Zabara, A.; Chong, J. T. Y.; Martiel, I.; Stark, L.; Cromer, B. A.; Speziale, C.; Drummond, C. J.; Mezzenga, R. Design of Ultra-Swollen Lipidic Mesophases for the Crystallization of Membrane Proteins with Large Extracellular Domains. *Nat. Commun.* **2018**, *9*, 1–9.

(11) Hua, T.; Vemuri, K.; Nikas, S. P.; Laprairie, R. B.; Wu, Y.; Qu, L.; Pu, M.; Korde, A.; Jiang, S.; Ho, J.-H.; et al. Crystal Structures of Agonist-Bound Human Cannabinoid Receptor CB1. *Nature* **2017**, *547*, 468–471.

(12) Landau, E. M.; Rosenbusch, J. P. Lipidic Cubic Phases: A Novel Concept for the Crystallization of Membrane Proteins. *Proc. Natl. Acad. Sci. U. S. A.* **1996**, *93*, 14532–14535.

(13) Amar-Yuli, I.; Adamcik, J.; Blau, S.; Aserin, A.; Garti, N.; Mezzenga, R. Controlled Embedment and Release of DNA from Lipidic Reverse Columnar Hexagonal Mesophases. *Soft Matter* **2011**, *7*, 8162–8168.

(14) Negrini, R.; Mezzenga, R. PH-Responsive Lyotropic Liquid Crystals for Controlled Drug Delivery. *Langmuir* **2011**, *27*, 5296–5303.

(15) Mezzenga, R.; Schurtenberger, P.; Burbidge, A.; Michel, M. Understanding Foods as Soft Materials. *Nat. Mater.* **2005**, *4*, 729–740.

(16) Sagalowicz, L.; Acquistapace, S.; Watzke, H. J.; Michel, M. Study of Liquid Crystal Space Groups Using Controlled Tilting with Cryogenic Transmission Electron Microscopy. *Langmuir* **2007**, *23*, 12003–12009.

(17) Esposito, E.; Carducci, F.; Mariani, P.; Huang, N.; Simelière, F.; Cortesi, R.; Romeo, G.; Puglia, C. Monoolein Liquid Crystalline Phases for Topical Delivery of Crocetin. *Colloids Surf. B Biointerfaces* **2018**, *171*, 67–74.
(18) Esposito, E.; Drechsler, M.; Puglia, C.; Cortesi, R. New Strategies for the Delivery of Some Natural Anti-Oxidants with Therapeutic Properties. *Mini Rev. Med. Chem.* **2019**.
(19) Barbosa, R. M.; Casadei, B. R.; Duarte, E. L.; Severino, P.; Barbosa, L. R. S.; Duran, N.; de Paula, E. Electron Paramagnetic Resonance and Small-Angle X-Ray Scattering Characterization of Solid Lipid Nanoparticles and Nanostructured Lipid Carriers for Dibucaine Encapsulation. *Langmuir ACS J. Surf. Colloids* **2018**, *34*, 13296–13304.
(20) Carducci, F.; Casadei, B. R.; Mariani, P.; Barbosa, L. R. S. X-Ray Characterization of Pharmaceutical and Cosmetic Lipidic Nanoparticles for Cutaneous Application. *Curr. Pharm. Des.* **2019**, *25*.
(21) Mazzoni, S.; Barbosa, L. R. S.; Funari, S. S.; Itri, R.; Mariani, P. Cytochrome-c Affects the Monoolein Polymorphism: Consequences for Stability and Loading Efficiency of Drug Delivery Systems. *Langmuir* **2016**, *32*, 873–881.
(22) Wang, H.; Zetterlund, P. B.; Boyer, C.; Spicer, P. T. Polymerization of Cubosome and Hexosome Templates to Produce Complex Microparticle Shapes. *J. Colloid Interface Sci.* **2019**, *546*, 240–250.
(23) Lv, F.; An, Z.; Wu, P. Scalable Preparation of Alternating Block Copolymer Particles with Inverse Bicontinuous Mesophases. *Nat. Commun.* **2019**, *10*, 1397.
(24) Zhai, J.; Fong, C.; Tran, N.; Drummond, C. J. Non-Lamellar Lyotropic Liquid Crystalline Lipid Nanoparticles for the Next Generation of Nanomedicine. *ACS Nano,* **2019**, *13*, 6178-6206.
(25) Luzzati, V.; Spegt, P. A. Polymorphism of Lipids. *Nature* **1967**, *215*, 701–704.
(26) Wang, X.; Zhang, Y.; Gui, S.; Huang, J.; Cao, J.; Li, Z.; Li, Q.; Chu, X. Characterization of Lipid-Based Lyotropic Liquid Crystal and Effects of Guest Molecules on Its Microstructure: A Systematic Review. *AAPS PharmSciTech* **2018**, *19*, 2023–2040.
(27) Mariani, P.; Luzzati, V.; Delacroix, H. Cubic Phases of Lipid-Containing Systems. Structure Analysis and Biological Implications. *J. Mol. Biol.* **1988**, *204*, 165–189.
(28) Hartl, C.; Frank, K.; Amenitsch, H.; Fischer, S.; Liedl, T.; Nickel, B. Position Accuracy of Gold Nanoparticles on DNA Origami Structures Studied with Small-Angle X-Ray Scattering. *Nano Lett.* **2018**, *18*, 2609–2615.
(29) Radaic, A.; Pugliese, G. O.; Campese, G. C.; Pessine, F. B. T.; Jesus, M. B. de; Radaic, A.; Pugliese, G. O.; Campese, G. C.; Pessine, F. B. T.; Jesus, M. B. de. Como estudar interações entre nanopartículas e sistemas biológicos. *Quím. Nova* **2016**, *39*, 1236–1244.
(30) Akhlaghi, S. P.; Ribeiro, I. R.; Boyd, B. J.; Loh, W. Impact of Preparation Method and Variables on the Internal Structure, Morphology, and Presence of Liposomes in Phytantriol-Pluronic(®) F127 Cubosomes. *Colloids Surf. B Biointerfaces* **2016**, *145*, 845–853.
(31) Glatter, O.; Kratky, O. *Small Angle X-Ray Scattering*; Academic Press: London, 1982.
(32) Guinier, A.; Fournet, G. *Small-Angle Scattering of X-Rays*; Wiley: London, 1955.
(33) Rizwan, S. B.; Dong, Y.-D.; Boyd, B. J.; Rades, T.; Hook, S. Characterisation of Bicontinuous Cubic Liquid Crystalline Systems of Phytantriol and Water Using Cryo Field Emission Scanning Electron Microscopy (Cryo FESEM). *Micron Oxf. Engl. 1993* **2007**, *38*, 478–485.

(34) Chountoulesi, M.; Pippa, N.; Pispas, S.; Chrysina, E. D.; Forys, A.; Trzebicka, B.; Demetzos, C. Cubic Lyotropic Liquid Crystals as Drug Delivery Carriers: Physicochemical and Morphological Studies. *Int. J. Pharm.* **2018**, *550*, 57–70.
(35) Briggs, J.; Caffrey, M. The Temperature-Composition Phase Diagram and Mesophase Structure Characterization of Monopentadecenoin in Water. *Biophys. J.* **1994**, *67*, 1594–1602.
(36) Tyler, A. I. I.; Barriga, H. M. G.; Parsons, E. S.; McCarthy, N. L. C.; Ces, O.; Law, R. V.; Seddon, J. M.; Brooks, N. J. Electrostatic Swelling of Bicontinuous Cubic Lipid Phases. *Soft Matter* **2015**, *11*, 3279–3286.
(37) Marsh, D. *Handbook of Lipid Bilayers*, 2nd ed.; CRC Press: Boca Raton, FL, USA, 2013.
(38) Bozzola, R. Monoolein and emulsions for internal use. *Boll Chim Farm* **1954**, *93*, 415–417.
(39) Strauss, E. W. Electron Microscopic Study of Intestinal Fat Absorption in Vitro from Mixed Micelles Containing Linolenic Acid, Monoolein, and Bile Salt. *J. Lipid Res.* **1966**, *7*, 307–323.
(40) Ericsson, B.; Larsson, K.; Fontell, K. A Cubic Protein-Monoolein-Water Phase. *Biochim. Biophys. Acta* **1983**, *729*, 23–27.
(41) Longley, W.; McIntosh, T. J. A Bicontinuous Tetrahedral Structure in a Liquid-Crystalline Lipid. *Nature* **1983**, *303*, 612–614.
(42) Qiu, H.; Caffrey, M. The Phase Diagram of the Monoolein/Water System: Metastability and Equilibrium Aspects. *Biomaterials* **2000**, *21*, 223–234.
(43) Barauskas, J.; Landh, T. Phase Behavior of the Phytantriol/Water System. *Langmuir* **2003**, *19*, 9562–9565.
(44) Akbar, S.; Anwar, A.; Ayish, A.; Elliott, J. M.; Squires, A. M. Phytantriol Based Smart Nano-Carriers for Drug Delivery Applications. *Eur. J. Pharm. Sci.* **2017**, *101*, 31–42.
(45) Esposito, E.; Carducci, F.; Mariani, P.; Huang, N.; Simelière, F.; Cortesi, R.; Romeo, G.; Puglia, C. Monoolein Liquid Crystalline Phases for Topical Delivery of Crocetin. *Colloids Surf. B Biointerfaces* **2018**, *171*, 67–74.
(46) Barriga, H. M. G.; Holme, M. N.; Stevens, M. M. Cubosomes; the next Generation of Smart Lipid Nanoparticles? *Angew. Chem. Int. Ed Engl.* **2019**, *58*, 2958-2978.
(47) Duttagupta, A. S.; Chaudhary, H. M.; Jadhav, K. R.; Kadam, V. J. Cubosomes: Innovative Nanostructures for Drug Delivery. *Curr. Drug Deliv.* **2016**, *13*, 482–493.
(48) Chen, J.-Y.; Su, C.-Y.; Hsu, C.-H.; Zhang, Y.-H.; Zhang, Q.-C.; Chang, C.-L.; Hua, C.-C.; Chen, W.-C. Solvent Effects on Morphology and Electrical Properties of Poly(3-Hexylthiophene) Electrospun Nanofibers. *Polymers* **2019**, *11*, 1501-1516.
(49) Magiera, A.; Marchelak, A.; Michel, P.; Owczarek, A.; Olszewska, M. A. Lipophilic Extracts from Leaves, Inflorescences and Fruits of Prunus Padus L. as Potential Sources of Corosolic, Ursolic and Oleanolic Acids with Anti-Inflammatory Activity. *Nat. Prod. Res.* **2019**, *Sept 18*, 1–6.
(50) Marchelak, A.; Owczarek, A.; Matczak, M.; Pawlak, A.; Kolodziejczyk-Czepas, J.; Nowak, P.; Olszewska, M. A. Bioactivity Potential of Prunus Spinosa L. Flower Extracts: Phytochemical Profiling, Cellular Safety, Pro-Inflammatory Enzymes Inhibition and Protective Effects Against Oxidative Stress In Vitro. *Front. Pharmacol.* **2017**, *8*, 680-694.
(51) Meli, V.; Caltagirone, C.; Falchi, A. M.; Hyde, S. T.; Lippolis, V.; Monduzzi, M.; Obiols-Rabasa, M.; Rosa, A.; Schmidt, J.; Talmon, Y.; et al. Docetaxel-Loaded Fluorescent Liquid-Crystalline Nanoparticles for Cancer Theranostics. *Langmuir ACS J. Surf. Colloids* **2015**, *31*, 9566–9575.

(52) Boulgaropoulos, B.; Rappolt, M.; Sartori, B.; Amenitsch, H.; Pabst, G. Lipid Sorting by Ceramide and the Consequences for Membrane Proteins. *Biophys. J.* **2012**, *102*, 2031–2038.
(53) Heftberger, P.; Kollmitzer, B.; Heberle, F. A.; Pan, J.; Rappolt, M.; Amenitsch, H.; Kucerka, N.; Katsaras, J.; Pabst, G. Global Small-Angle X-Ray Scattering Data Analysis for Multilamellar Vesicles: The Evolution of the Scattering Density Profile Model. *J. Appl. Crystallogr.* **2014**, *47*, 173–180.
(54) Santiago, G. M. P.; Viana, F. A.; Pessoa, O. D. L.; Santos, R. P.; Pouliquen, Y. B. M.; Arriaga, A. M. C.; Andrade-Neto, M.; Braz-Filho, R. Avaliação Da Atividade Larvicida de Saponinas Triterpênicas Isoladas de Pentaclethra Macroloba (Willd.) Kuntze (Fabaceae) e Cordia Piauhiensis Fresen (Boraginaceae) Sobre Aedes Aegypti. *Rev. Bras. Farmacogn.* **2005**, *15*, 187–190.
(55) Banov, D.; Banov, F.; Bassani, A. S. Case Series: The Effectiveness of Fatty Acids from Pracaxi Oil in a Topical Silicone Base for Scar and Wound Therapy. *Dermatol. Ther.* **2014**, *4*, 259–269.